INT. J. REMOTE SENSING, 2002, VOL. 23, NO. 2, 371–387

Taylor & Francis
Taylor & Francis Group

Accounting for spatial dependence in the processing of multi-temporal SAR images using factorial kriging

M. VAN MEIRVENNE

Department of Soil Management and Soil Care, Ghent University, Coupure 653, 9000 Ghent, Belgium; e-mail: Marc.Vanmeirvenne@rug.ac.be

and P. GOOVAERTS

Department of Civil and Environmental Engineering, The University of Michigan, EWRE building, Ann Arbor, Michigan 48109-2125, USA; e-mail: goovaert@engin.umich.edu

(*Received 9 September 1999; in final form 26 June 2000*)

Abstract. The interpretation or classification of multi-temporal satellite images that share large portions of redundant information can generally be improved by principal component analysis (PCA). A shortcoming of PCA is that the spatial structure of the images is ignored. Spatial variability often consists of several nested levels of variance and their blending could mask information that is dominant at a specific level or spatial scale. Factorial kriging (FK) is a geostatistical technique that allows the filtering of spatial components identified from nested variograms and is here used to extract scale-dependent information from satellite images prior to PCA. The benefit of this geostatistical pre-processing of multi-temporal images is investigated using a winter sequence of eight European Remote Sensing (ERS 1/2) Synthetic Aperture Radar (SAR) images. Each image was processed by FK to isolate the variation present at a 'regional' scale (between 289 and 700 m) prior to a PCA of the filtered images. Compared to an earlier study where PCA was performed on the original images, filtering enhanced the relation between the first three principal components and land characteristics associated with topography, soil drainage conditions and land use.

1. Introduction

The study of multi-temporal satellite images allows one to investigate the spatial variability and temporal dynamics of the physical and biological factors influencing the registered signal. To improve the interpretation of a series of images that contain a large proportion of redundant information, multivariate statistical techniques, like PCA, are commonly used (Richards 1986). A shortcoming of these techniques is that the structure of the spatial (or temporal) variation of the controlling factors is ignored. Nevertheless, land characteristics like landform, soil and vegetation, often display some degree of spatial autocorrelation, reflected in the satellite images. Moreover, multiple levels of autocorrelation may exist, each acting at a different spatial scale, and their identification would allow one to focus on any particular scale, i.e. to filter out all other contributing levels from the signal. Principal component analysis of the filtered images would possibly improve their interpretation.

International Journal of Remote Sensing
ISSN 0143-1161 print/ISSN 1366-5901 online © 2002 Taylor & Francis Ltd
http://www.tandf.co.uk/journals
DOI: 10.1080/01431160010014800

Factorial kriging FK is a geostatistical method developed by Matheron (1982) to decompose a signal into different spatial components on the basis of a nested variogram model. It has been shown that FK in the spatial domain is equivalent to spectral analysis in the frequency domain (Galli and Sandjivy 1985). Although the application of FK is not new to earth sciences (e.g. Galli *et al.* 1984, Wackernagel 1988, Goovaerts 1992), it was rarely used to investigate multi-temporal remotely sensed images. Two exceptions are the work by Ma and Royer (1988) on image restoration, filtering and lineament enhancement by factorial kriging, and an analysis of sonar images by Wen and Sinding-Larsen (1997).

The major objective of this paper was to investigate whether performing FK prior to PCA would improve the interpretation of multi-temporal images. The approach was illustrated using the data presented in a recent paper by Verhoest *et al.* (1998), who analysed a winter sequence of eight SAR images taken by ERS 1 and 2 satellites, summarizing the information contained in the SAR images into three principal components (PCs). They showed that these three PCs could be related (in decreasing order of explained variance) to the local incidence angle calculated from a digital elevation model, the soil drainage conditions derived from a soil map, and a land use and land cover image obtained from a classified Landsat image.

2. Theory

2.1. *Nested variation*

The structure of spatial variation of observations z of a random function Z is commonly described by the semivariance γ, estimated as (Goovaerts 1997):

$$\gamma^*(\mathbf{h}) = \frac{1}{2n(\mathbf{h})} \sum_{\alpha=1}^{n(\mathbf{h})} [z(\mathbf{x}_\alpha) - z(\mathbf{x}_\alpha + \mathbf{h})]^2 \tag{1}$$

where $n(\mathbf{h})$ is the number of pairs of observations made at locations $\mathbf{x}_\alpha$ and $(\mathbf{x}_\alpha + \mathbf{h})$, separated by a vector $\mathbf{h}$. The plot of $\gamma^*(\mathbf{h})$ versus $\mathbf{h}$, called a variogram, describes the spatial variation in terms of magnitude, scale and pattern. Variograms of remotely sensed images were first calculated by Curran (1988) and Woodcock *et al.* (1988) and have been frequently encountered in literature since then.

Whenever measurements are taken over a large area, as it is the case with the SAR images used in this study, several, say $L+1$, levels of variation could be encountered, leading to so-called nested variograms that display different structures (e.g. different ranges of spatial dependence). Variograms are thus modelled as the sum of $L+1$ basic variograms, each corresponding to a distinct spatial structure:

$$\gamma(\mathbf{h}) = \sum_{l=0}^{L} \gamma_l(\mathbf{h}) = \sum_{l=0}^{L} b_l g_l(\mathbf{h}) \quad \text{with } b_l \geqslant 0 \tag{2}$$

where b_l is the variance of the corresponding basic variogram model $g_l(\mathbf{h})$. Conventionally, the variance corresponding to $l=0$ is called a nugget and represents the spatially unstructured part of the total variance. Based on the linear model of regionalization (equation (2)), the random function $Z(\mathbf{x})$ can be decomposed into a sum of $(L+1)$ independent random functions, called spatial components, and its local mean $m(\mathbf{x})$:

$$Z(\mathbf{x}) = \sum_{l=0}^{L} Z_l(\mathbf{x}) + m(\mathbf{x}) \tag{3}$$

where $Z_l(\mathbf{x})$ is the lth spatial component corresponding to the variogram model $g_l(\mathbf{h})$.

2.2. *Factorial kriging*

Factorial kriging is a variant of kriging that aims to map each spatial component individually, which amounts at filtering out the L other components. The estimator of the lth spatial component of variable Z at location $\mathbf{x}_0$ is (Goovaerts 1997):

$$Z_l^*(\mathbf{x}_0) = \sum_{\alpha=1}^{n} \lambda_{\alpha,l} Z(\mathbf{x}_\alpha) \tag{4}$$

with n the number of neighbouring observations around $\mathbf{x}_0$ involved in the estimation, each receiving a weight $\lambda_{\alpha,l}$. Because the available observations $z(\mathbf{x}_\alpha)$ contain the contributions of all $L+1$ components which are considered mutually independent, only the contribution of the lth component must be taken into account in the right-hand side term of the kriging system. Moreover to ensure unbiasedness and provided the variogram model $g_l(\mathbf{h})$ is bounded (stationary case), the kriging weights $\lambda_{\alpha,l}$ must sum to zero, and not to one as in ordinary kriging (Wackernagel 1998, p. 114). This leads to the following kriging system for the lth component:

$$\begin{cases} \sum_{\beta=1}^{n} \lambda_{\beta,l} \gamma(\mathbf{x}_\alpha - \mathbf{x}_\beta) + \phi_l = b_l g_l(\mathbf{x}_\alpha - \mathbf{x}_0) & \text{for } \alpha = 1, \ldots, n \\ \sum_{\beta=1}^{n} \lambda_{\beta,l} = 0 \end{cases} \tag{5}$$

where ϕ_l is the Lagrange multiplier for the lth component. This system of $n+1$ equations must be solved to find the n weights $\lambda_{\alpha,l}$ that are then inserted into equation (4) to estimate the lth spatial component of variable Z at location $\mathbf{x}_0$. The operation is repeated for all locations where such a decomposition is required.

For remotely sensed images the number of observations (pixels) around $\mathbf{x}_0$ is typically large. Hence, when one wishes to estimate a large-scale component, the closest pixels could screen the more distant ones. As a result, the size of the search neighbourhood that actually contributes to the estimate can be much smaller than the range of the component to be estimated (Goovaerts and Webster 1994). To overcome this problem encountered during the reproduction of large-scale features we used Jaquet (1989)'s procedure that consists of adding the local mean $m(\mathbf{x}_0)$ to the long-range component $z^*_{(L+1)}(\mathbf{x}_0)$. The latter is estimated as:

$$m^*(\mathbf{x}_0) = \sum_{\alpha=1}^{n} \lambda_{\alpha,m} Z(\mathbf{x}_\alpha) \tag{6}$$

The weights, $\lambda_{\alpha,m}$, used to derive the local mean can be obtained by solving the following kriging system (Goovaerts 1997):

$$\begin{cases} \sum_{\beta=1}^{n} \lambda_{\beta,m} \gamma(\mathbf{x}_\alpha - \mathbf{x}_\beta) + \phi_m = 0 & \text{for } \alpha = 1, \ldots, n \\ \sum_{\beta=1}^{n} \lambda_{\beta,m} = 1 \end{cases} \tag{7}$$

2.3. *Principal component analysis*

Principal component analysis of a set of p images generally aims to summarize—and hopefully improve the interpretation of—the available information by a few, say k, new images that are orthogonal linear combinations of the original images, referred to as PCs. The analysis requires the computation of the eigenvalues and eigenvectors

of the variance–covariance matrix (or the correlation matrix) of the p images. The eigenvectors determine the directions of maximum variability while the eigenvalues specify the variances of the vectors. The mathematical details of PCA can be found in standard textbooks (e.g. Johnson and Wichern 1992).

The first principal component 'explains' the largest part of the total variance included in all p images, the second component the second largest part, etc. The larger the correlation between the p images, the fewer the k components required to explain a large part of the total variance of the original images. For this reason, PCA is a common method to improve the interpretation and classification of multi-spectral or multi-temporal satellite images (Richards 1986, Lillesand and Kiefer 1994). Principal component analysis has been used on multifrequency SAR images by Lee and Hoppel (1992) and on multi-temporal images by Henebry (1997) and Verhoest *et al.* (1998).

3. SAR images

Active microwave (radar) signals have the advantage of having a penetrating power and their degree of backscatter depends on their interaction with surface roughness, soil moisture (depending on the dielectric constant of the soil) and vegetation (Ulaby *et al.* 1982). Research has thus been conducted to investigate the use of use radar backscattering to obtain information on soil moisture patterns, either through direct inversion of the obtained signal (e.g. Lin *et al.* 1994) or through a multi-temporal processing of several images (e.g. Gineste *et al.* 1998).

We obtained eight SAR images already pre-processed, i.e. georeferenced, calibrated and Gamma MAP (Lopes 1990) speckle filtered, as described in detail by Verhoest *et al.* (1998). These images were taken from the Zwalm catchment (located in the centre of Belgium) during the winter of 1995–1996 by the ERS 1 and 2 satellites put in a 'tandem-phase' at a nominal altitude of 785 km. This resulted in four pairs of ERS 1/2 images observed at an exact time interval of 24 h. These image pairs were taken on 31 October/1 November 1995, 5/6 December 1995, 13/14 February 1996 and 19/20 March 1996. In the subsequent text we will identify these images chronologically as I1 to I8 and we will refer to them as the original images. The SAR was a C band (5.3 GHz) working in vertical–vertical polarization with a pixel size of 12.5 by 12.5 m resampled to a resolution of 30 m by 30 m.

4. Results

4.1. *Transformation*

Methods based on second-order moments of distributions, like PCA, are sensitive to skewed data. Since the digital numbers of the SAR images were found to be highly positively skewed, the images were logarithmically ($\ln_e$) transformed and all subsequent analyses were carried out on these transformed data.

4.2. *Variograms*

Directional variograms (E–W, NE–SW, N–S and NW–SE) were calculated (equation (1)) for all eight transformed SAR images. Only small differences were found between these four major directions, and the remaining analysis was performed on the omnidirectional variograms. The variograms of the eight images were very similar and therefore the same set of basic models was fitted to all eight variograms using a weighted least-squares regression. The model consisted of a nugget component and two nested exponential models (equation (2)):

- $g_0(\mathbf{h})=0 \quad \text{if } \mathbf{h}=0;\ g_0(\mathbf{h})=1 \quad \text{if } \mathbf{h}>0;$
- $g_1(\mathbf{h})=1-\exp\left(\frac{-3\mathbf{h}}{a_1}\right) \quad \text{if } \mathbf{h}>0;$
- $g_2(\mathbf{h})=1-\exp\left(\frac{-3\mathbf{h}}{a_2}\right) \quad \text{if } \mathbf{h}>0$

where the practical ranges a_1 and a_2 are equal to 289 m and 700 m respectively. The coefficients b_l (equation (2)) are listed in table 1 and the corresponding eight variograms are shown in figure 1. The high degree of similarity between all variograms suggests a dominance of similar features on the backscattering at all recorded dates. Note as well that despite the images have been filtered for speckle, the nugget variance is still considerable: between 13.9 and 27.0% of the total variance of the images (as can be calculated from table 1).

4.3. *Factorial kriging*

FK was performed on all eight images isolating each of the three spatial components (nugget, local and regional). Figure 2 shows the original SAR image I1, together with images of its decomposed nested structures. The image of the first structure (*b*) reveals an uncorrelated 'salt and pepper' pattern, which can be largely identified as the remaining noise after speckle filtering. The second structure (*c*) shows features displaying some continuity at a detailed scale (< 289 m), which we term 'local', but it is unclear which characteristics these represent. The image of the third structure (*d*) (289 to 700 m), termed 'regional', shows indications of larger scale land characteristics, like communities and forested areas. However, their identification remains unclear. We therefore proceeded with PCA of the eight images of the regional structure.

4.4. *Principal component analysis of the regional structure*

The eight images of the regional structure were subject to PCA. This analysis was performed on standardized variables (i.e. based on the eigenvalues and eigenvectors of the correlation matrix) to eliminate differences in the average digital numbers caused by the calibration of the images. The first PC accounted for 96.4% of the total variance, the second for 1.51% and the third for 0.74%. These results indicate

Table 1. Coefficients b_l of the fitted linear model of regionalization to the eight variograms of the logtransformed SAR images.

Image	b_0	b_1	b_2
I1	0.0117	0.0375	0.005576
I2	0.0120	0.0361	0.004265
I3	0.0113	0.0274	0.004810
I4	0.0118	0.0275	0.004333
I5	0.0089	0.0432	0.011886
I6	0.0101	0.0324	0.010562
I7	0.0091	0.0390	0.007477
I8	0.0099	0.0375	0.006571

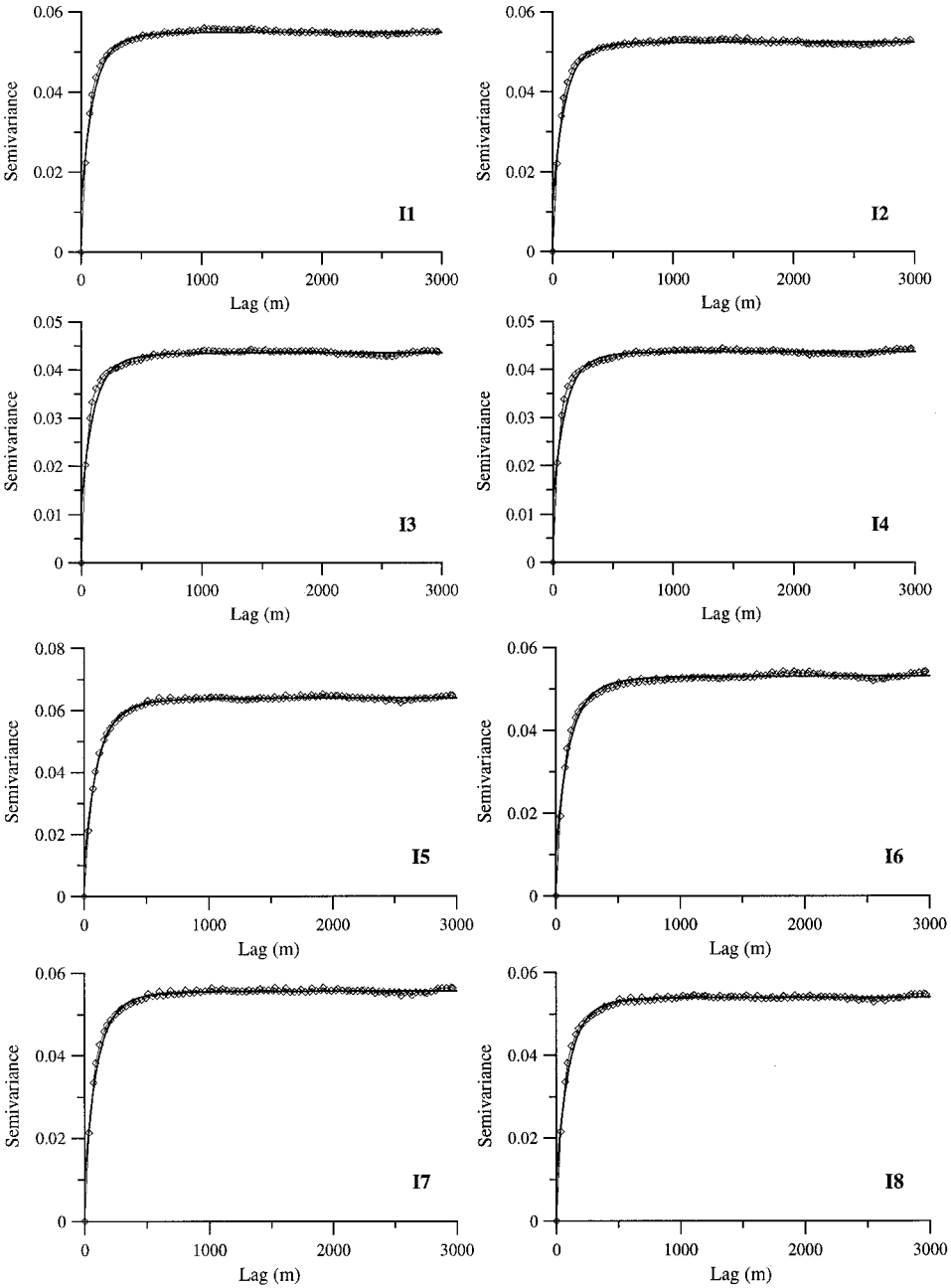

Figure 1. Omnidirectional experimental (dots) and theoretical (solid curves) variograms of the eight original SAR images (I1 to I8).

the large portion of redundant information present in the SAR images on a regional scale. The images of the first three PCs obtained in this way are shown in figures 3(*b*), 4(*b*) and 5(*b*), together with the first three PCs obtained from the original images (figures 3(*c*), 4(*c*) and 5(*c*)).

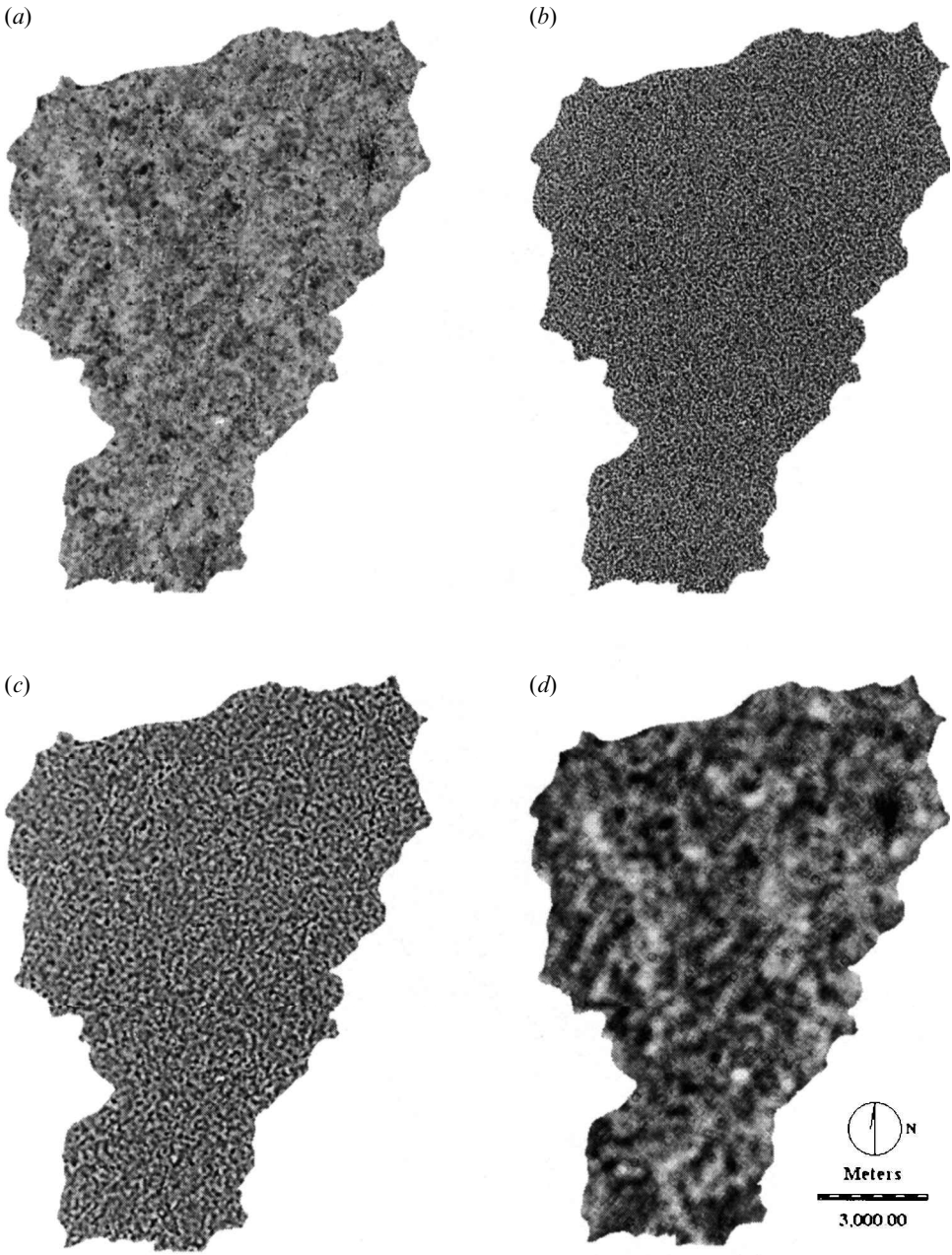

Figure 2. Original SAR image I1 (*a*) and its decomposition by FK into three structures: (*b*) nugget; (*c*) local; (*d*) regional.

4.5. *Physical land characteristics*

The first three PCs of the SAR images could be linked to three land characteristics:

- the local incidence angle (which was the same for all images) as calculated from a digital elevation model of the catchment area, representing its topographic slopes;

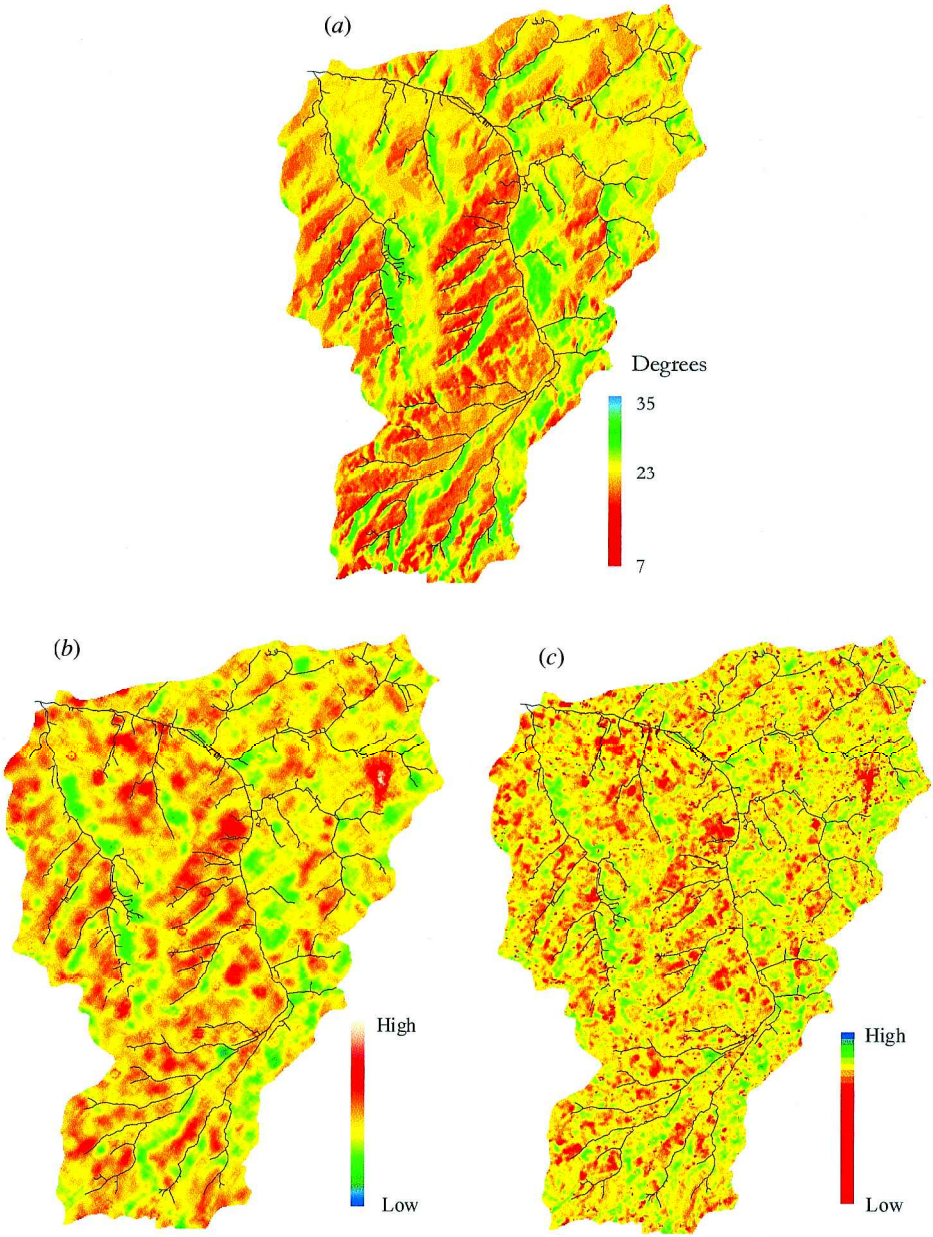

Figure 3. Images of (*a*) local incidence angle, (*b*) first PC of the regional structure and (*c*) first PC of the original SAR images (Verhoest *et al.* 1998). The river network was added as reference (black). The colour scale was defined differently on each image to obtain the best comparable colour composition.

- classes of soil drainage conditions, representing average soil moisture conditions during the winter period;
- classes of land use and land cover, representing the average vegetative cover during the observation period.

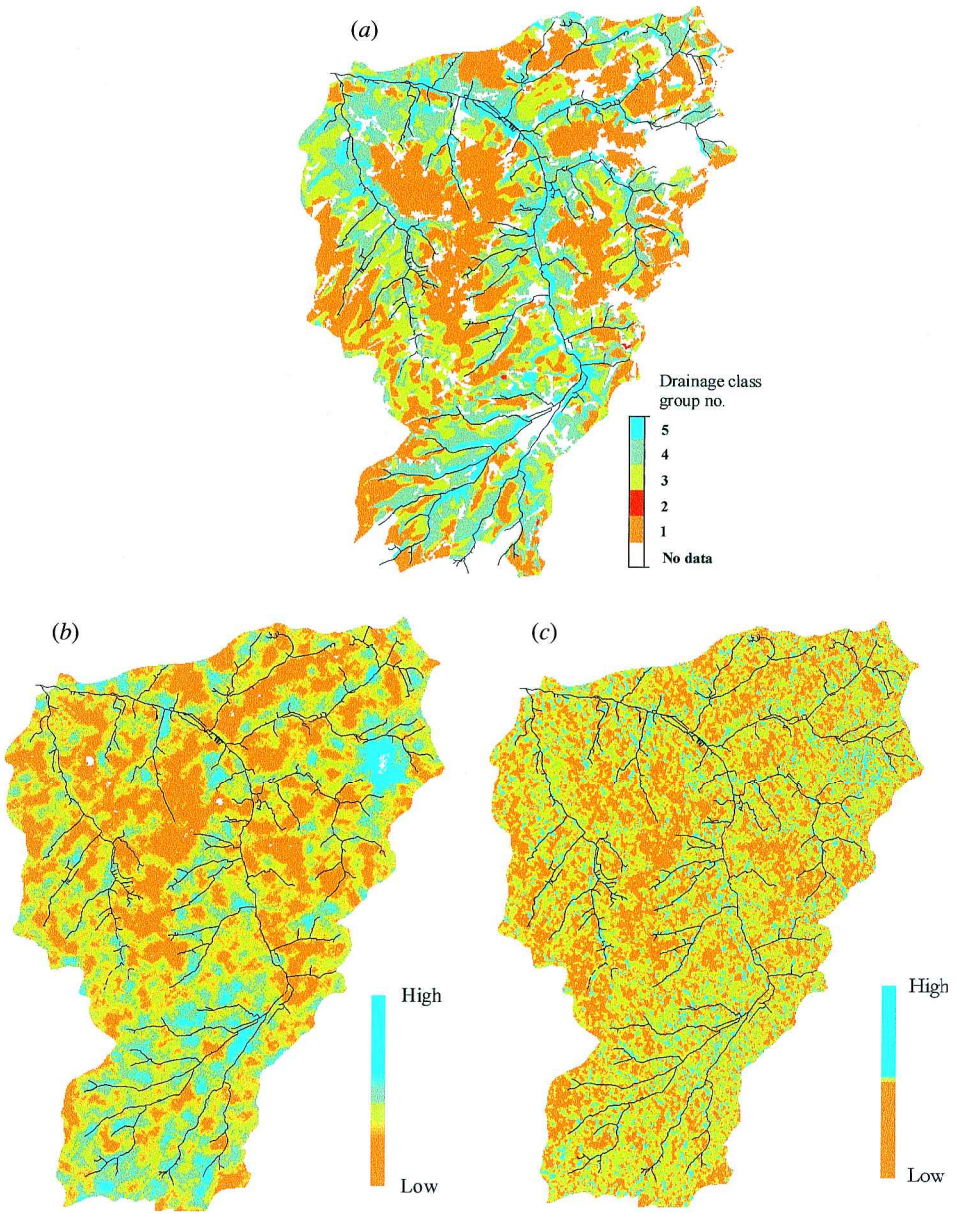

Figure 4. Images of (*a*) grouped drainage classes, (*b*) second PC of the regional structure and (*c*) second PC of the original SAR images (Verhoest *et al.* 1998). The colour scale was defined differently on each image to obtain the best comparable colour composition.

The first PC of the regional structure (figure 3(*b*)) is very similar to the image of the local incidence angle (figure 3(*a*)), highlighting the dominant effect of topography on the SAR signal. Slopes oriented towards the satellites have a smaller local incidence angle than those on the opposite sides of the valleys. Consequently their backscattering will be larger on all images. The clear improvement obtained by isolating the regional structure versus the first PC of the original SAR images

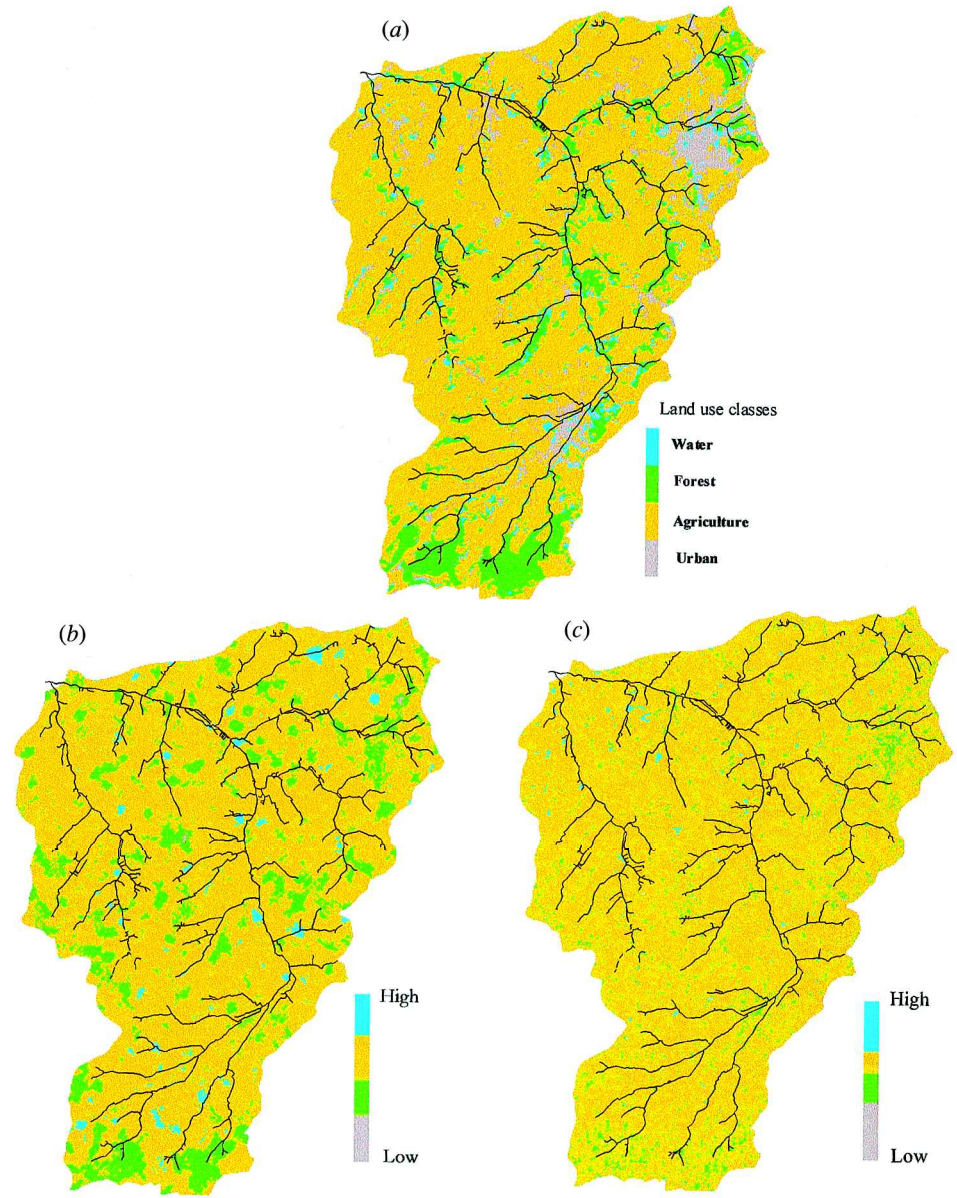

Figure 5. Images of (*a*) grouped land use and land cover classes, (*b*) third PC of the regional structure and (*c*) third PC of the original SAR images (Verhoest *et al.* 1998).

(figure 3(*c*)) reflects the regional scale at which the topography influences the radar signal.

Figure 4 compares the second PCs, obtained with and without FK filtering, with a rasterized image of the drainage classes extracted from the Belgian soil map (original scale: 1:20 000). The soil map legend indicates nine drainage classes within the Zwalm catchment, but we combined these into five categories to obtain more clearly distinguishable groups. Table 2 defines the groups of drainage classes in terms of winter water table conditions, since the SAR images were taken during the winter.

Table 2. Definitions of the groups of soil drainage classes in terms of winter water table conditions.

Group no.	Drainage classes	Average winter water table depth (cm below surface)
1	b	>125
2	A	>50
3	c	80–125
4	d and D	50–125
5	e, h, f and g	0–50

The driest soils (group no. 1) cover 36.9% of the watershed, whereas the wettest soils (group no. 5) cover 9.9%. The soils with the poorest drainage (groups 4 and 5) are mainly located along the river network and in the valleys. A similar pattern can be observed on the image of the second PC of the regional structures (figure 4(*b*)), and less clearly on the image of the second PC of the original images (figure 4(*c*)). This result supports the findings of Verhoest *et al.* (1998) who reported a relationship between soil moisture behaviour on a catchment scale and the second PC of the SAR images. Urban areas (see figure 5(*a*), indicated as 'no data' on figure 4(*a*)) were not mapped by the soil surveyors, but they show up very clearly on the second PC of the regional structure.

The third PC was compared to a land use and land cover image (figure 5(*a*)) obtained from a supervised classification of a Landsat image taken on 12 October 1994. Ten classes of land use and land cover were originally identified, but they were grouped into four classes: agriculture, forest, urban and water (listed in declining order of spatial extension). Similarly to soil moisture conditions, typical backscattering will appear when land use remained consistent during the observed period, which is realistic during the winter season. Generally, the third PC shows some similarity with land use, suggesting some influence on the SAR backscattering. In particular, the forests in the south of the catchment were clearly reproduced on the image of the third PC of the regional structure. Variations remain, however, especially for agricultural areas, which may be due to the small dimensions of parcels (on average about 1.5 ha) encountered in the catchment. Because of the presence of large differences in vegetative cover on agricultural land (from bare to permanent pasture), the detection of these parcels is difficult on the PC extracted from the images of the regional structure. Therefore, we repeated PCA on the combined images of the local and regional structures (thus filtering only the noise). Because the visual discretization of land use and the relationship with ground measurements (see §4.6) were not improved, further discussion is restricted to the PCs of the regional structures.

4.6. *Quantification of the relationships*

The closeness of two images was assessed by the coefficient of determination r^2 and assessment of the similarity of the variograms as follows.

- The coefficient of determination r^2 (Wonnacott and Wonnacott 1990) measures the strength of the relationship on a pixel-by-pixel basis. This coefficient was obtained either from regression analysis when two quantitative images were compared, or by an analysis of variance when one of the images was categorical. r^2 is the ratio of the explained sum of squares to the total sum of squares and

so represents the proportion of the total variation accounted for by the regression or classification.

- The similarity of the variograms of both images describes the patterns of spatial variation. We standardized the experimental variograms to a common sill to facilitate their comparison, since there is no measure available to quantify similarity between variograms (Boucneau *et al.* 1998).

The r^2 between the local incidence angle and the first PC of the regional structures (figure 3) was 0.251 (table 3), which is considerably higher than the r^2 of 0.079 obtained when the local incidence angle was compared with the first PC of the original images. To investigate the effect of the logarithmic transformation, PCA was performed on the logtransformed SAR images without FK filtering, yielding a r^2 of 0.122 between the first PC and the local incidence angle. This result indicated the importance of reducing the skewness of the histograms of digital numbers before proceeding with methods based on second-order moments, but it also suggested that the major gain resulted from FK filtering. In absolute terms an r^2 of 0.251 is still rather small, but figure 3 shows the strong visual similarity between both images. The limitation of r^2 is its calculation on a pixel-by-pixel basis, which amounts to ignoring any spatial correlation between neighbouring observations, although this feature is responsible for the strong visual resemblance between both images. Hence, it is worth including a measure of spatial structure, such as the variogram, into the comparison.

The r^2 between the second and third PCs and the soil drainage classes and land use classes respectively, also increased when the SAR images were filtered to isolate regional structure (table 3). However, the values remain very low, notwithstanding the observable similarities (figures 4 and 5).

The experimental variograms of the local incidence angle displayed strongly anisotropic behaviour (figure 6(*a*)) with the slowest increase in spatial variability along the NE–SW direction. The steepest increase was found in the E–W and NW–SE directions. Such an anisotropy corresponds to the preferential orientation of the valleys to the NE–SW that causes less variation of the local incidence angle over short distances in this direction. A similar anisotropy was found for the directional variograms of the first PC of the regional structure (figure 6(*b*)) whereas the spatial pattern of the PC of the original images (figure 6(*c*)) was direction-independent.

Since the soil drainage and land use maps are categorical, equation (1) cannot be used directly to characterize their spatial variability. A prior coding of each pixel

Table 3. Coefficients of determination (r^2) between the land characteristics and the images of the different analyses.

	PCs obtained from the original SAR images	PCs of the images of the regional structure obtained by FK	
		PC 1	
Local incidence angle	0.079		0.251
		PC 2	
Drainage classes	0.025		0.062
		PC 3	
Land use classes	0.021		0.050

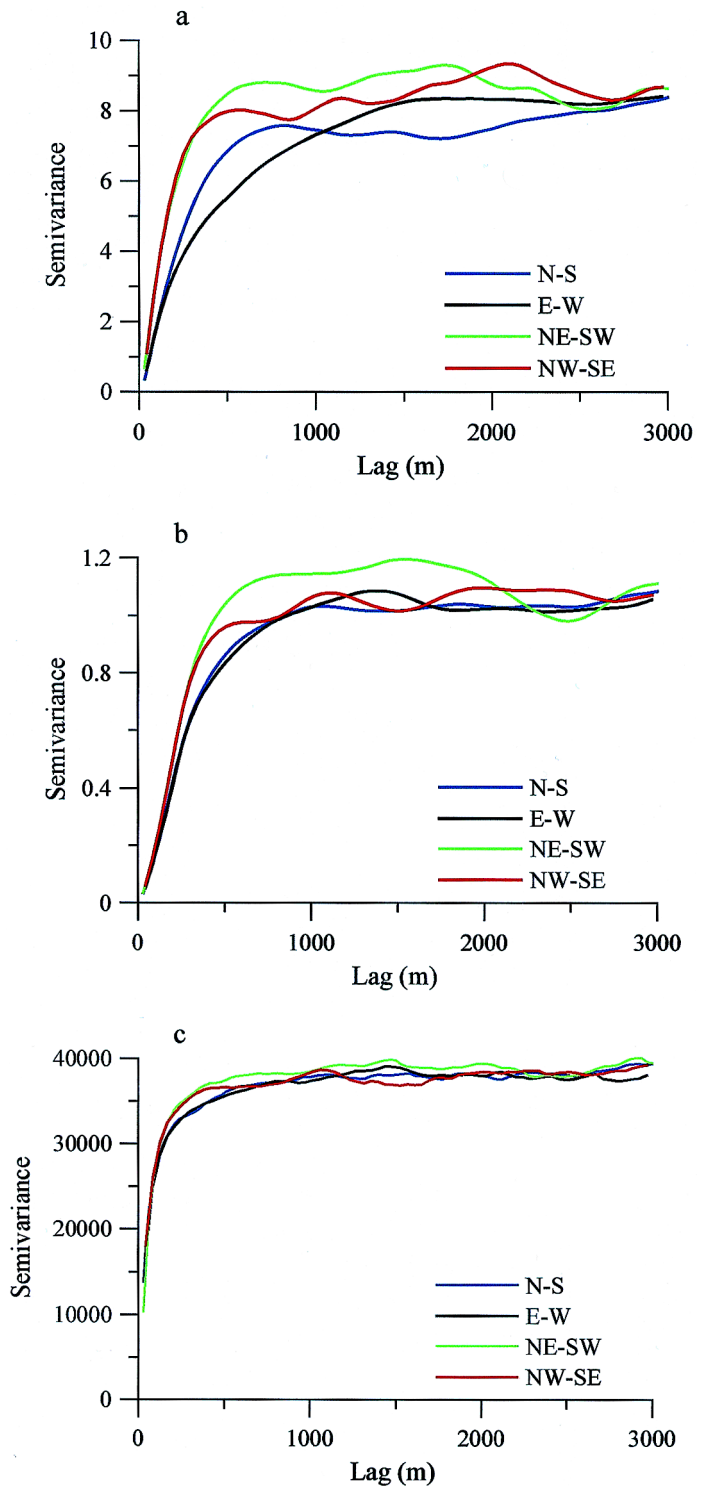

Figure 6. Four-directional experimental variograms of the images of (*a*) local incidence angle, (*b*) first PC of the regional structure and (c) first PC of the original SAR images.

$\mathbf{x}_\alpha$ into an indicator of the presence or absence of the different categories is required (Goovaerts and Webster 1994, Lark and Beckett 1998). Suppose that there are K categories c_k $(k=1, \ldots, K)$ within an image, then each location $\mathbf{x}_\alpha$ is coded into a vector of K indicator values defined as:

$$i(\mathbf{x}_\alpha; c_k) = \begin{cases} 1 & \text{if } \mathbf{x}_\alpha \in c_k \\ 0 & \text{otherwise} \end{cases} \qquad k=1, \ldots, K \tag{8}$$

The probability, $p(\mathbf{h})$, that two pixels, separated by $\mathbf{h}$, belong to different categories is calculated by:

$$p(\mathbf{h}) = \sum_{k=1}^{K} \left\{ \frac{1}{2n(\mathbf{h})} \sum_{\alpha=1}^{n(\mathbf{h})} [\, i(\mathbf{x}_\alpha; c_k) - i(\mathbf{x}_\alpha + \mathbf{h}; c_k)]^2 \right\} \tag{9}$$

This function is also called the sum of indicator variograms (SIV).

We calculated the SIV of the soil drainage map (figure 4(*a*)) and compared it with the variograms of the second PC of the regional structure (figure 4(*b*)) and of the original SAR images (figure 4(*c*)). All these variograms were isotropic and they were standardized to a common sill to facilitate their comparison (figure 7). The variogram of the PC of the regional structure much more closely resembled the SIV of the soil drainage map, suggesting some degree of spatial similarity between both images, notwithstanding the small r^2. The variogram of the second PC of the original SAR images differed more significantly from the SIV of the soil drainage classes: it had a much larger nugget and a nested structure with a very short first range.

The standardized SIV of the land use map (figure 5(*a*)) is shown in figure 8, together with the standardized omnidirectional variograms of the third PC of the regional structure (figure 5(*b*)) and of the original SAR images (figure 5(*c*)). None of the two PC variograms looked like the SIV of land use classes, except for the nugget effect that was more similar for the regional structure. This indicates that at least

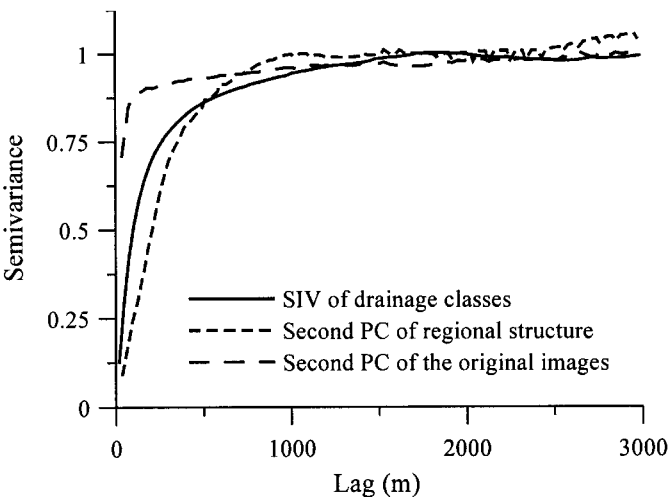

Figure 7. Omnidirectional SIV of the soil drainage classes, omnidirectional variograms of the second PC of the regional structure and of the original SAR images, all standardized to a unit sill.

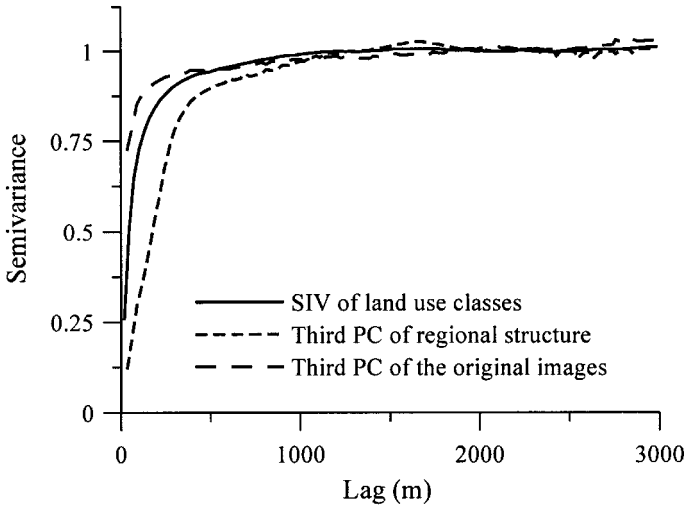

Figure 8. Omnidirectional SIV of the land use classes, omnidirectional variograms of the third PC of the regional structure and of the original SAR images, all standardized to a unit sill.

the noise was successfully removed by FK, but that the spatial patterns of land use could not be satisfactorily described.

5. Discussion and conclusions

The histograms of the eight SAR images were strongly positively skewed, calling for a logarithmic transformation to reduce the influence of extreme values. The variograms of the images were all very similar with a large nugget variance. Two nested spatial structures with ranges of 289 m and 700 m were identified. FK was used to filter the nugget and the first nested structure, yielding maps of the regional structure (to which the local mean was added). A PCA of these filtered images indicated that the first PC contained the majority of information (96.4% of total variance) while the second and third PCs accounted only for 1.51 and 0.74% respectively. So, the multi-temporal images were found to be very similar, both in their information content and in their spatial structure.

For the first PC, a strong visual relationship with the local incidence angle, representing topography, was confirmed by an r^2 of 0.251, whereas it was 0.079 when no decomposition was conducted and 0.122 when only a logtransformation of the digital numbers was performed. Moreover, a comparison of the variograms indicated that the anisotropic behaviour of the local incidence angle was largely reproduced by the PC of the regional structure, but not by the PC of the original images. This result confirms the improvement quantified by r^2, but also suggests that filtering by FK strengthens the spatial relationship (in terms of spatial continuity) between the SAR signal and topography.

Some analogy could be visually observed between the second PC of the regional structure and the soil drainage map, providing information about the average soil moisture status. Although the r^2 increases after filtering, it remained very small (0.062). However, a comparison of the SIV of the soil drainage classes with the variograms of second PCs of the filtered and original images indicated a stronger

spatial similarity for the regional structure, suggesting that the sequence of SAR images captured the dynamics of soil moisture throughout this winter period better on a regional scale than at a finer resolution. Additionally, urban areas were most clearly observed on the image of the second PC.

The relationship between the third PC of the regional structure and the land use map (vegetation cover) was less apparent. The r^2 increased by FK filtering but remained very small (0.050). This improvement was not clearly confirmed by the variogram comparison. It seems that the impact of land use and land cover is not restricted to a single spatial scale, although the noise filtering enhanced the similarity with the nugget of the SIV of land use classes.

In summary, we have shown that geostatistical methods, like FK and variogram analysis, which are based on the explicit quantification of the spatial dependence within images, can improve the extraction of information from multi-temporal SAR images. Further research is, however, needed to enhance the ability of multi-temporal SAR images to predict land characteristics.

Acknowledgments

We express grateful thanks to N. Verhoest, P. Troch and F. De Troch for providing data from their research. This research was funded by the TELSAT 4 programme (project no. T4/02/33) granted by the Federal Services for Scientific, Technical and Cultural Affairs (DWTC). It was partly conducted during a leave of the first author at The University of Michigan for which he gratefully acknowledges the financial support of the Flemish Fund for Scientific Research (FWO).

References

Boucneau, G., Van Meirvenne, M., Thas, O., and Hofman, G., 1998, Integrating properties of soil map delineations into ordinary kriging. *European Journal of Soil Science*, **49**, 213–229.

Curran, P. J., 1988, The semivariogram in remote sensing: an introduction. *Remote Sensing of Environment*, **24**, 493–507.

Galli, A., Gerdil-Neuillet, F., and Dadou, C., 1984, Factorial kriging analysis: a substitute to spectral analysis of magnetic data. In *Geostatistics for Natural Resources Characterization*, edited by G. Verly, M. David, A. Journel and A. Marechal (Dordrecht: Reidel), pp. 543–557.

Galli, A., and Sandjivy, L., 1985, Analyse krigeante et analyse spectrale. *Sciences de la Terre, Série Informatique*, **21**, 115–124.

Gineste, P., Puech, C., and Mérot, P., 1998, Radar remote sensing of the source areas from the Coët-Dan catchment. *Hydrological Processes*, **12**, 267–284.

Goovaerts, P., 1992, Factorial kriging analysis: a useful tool for exploring the structure of multivariate spatial soil information. *Journal of Soil Science*, **43**, 597–619.

Goovaerts, P., 1997, *Geostatistics for Natural Resources Evaluation,* (New York: Oxford University Press).

Goovaerts, P., and Webster, R., 1994, Scale-dependent correlation between topsoil copper and cobalt concentrations in Scotland. *European Journal of Soil Science*, **45**, 79–95.

Henebry, G. M., 1997, Advantages of principal component analysis for land cover segmentation from SAR image series. *Proceedings of 3rd ERS Symposium on Space at the Service of our Environment, 14–21 March 1997, Florence, Italy*, (Noordwijk: European Space Agency Publications), pp. 175–178.

Jaquet, O., 1989, Factorial kriging analysis applied to geological data from petroleum exploration. *Mathematical Geology*, **21**, 683–691.

Johnson, R. A., and Wichern D. W., 1992, *Applied Multivariate Statistical Analysis* (London: Prentice-Hall).

LARK, R. M., and BECKETT P. H. T., 1998. A geostatistical descriptor of the spatial distribution of soil classes, and its use in predicting the purity of possible soil map units. *Geoderma*, **83**, 243–267.

LEE, J., and HOPPEL K., 1992, Principal components transformation of multifrequency polarimetric SAR imagery. *IEEE Transactions on Geoscience and Remote Sensing*, **30**, 686–696.

LILLESAND, T. M., and KIEFER, R. W., 1994, *Remote Sensing and Image Interpretation*, third edition (New York: Wiley).

LIN, D. S., WOOD, E. F., TROCH, P. A., MACINI, M., and JACKSON, T. J., 1994, Comparison of remote sensed and model simulated soil moisture over a heterogeneous watershed. *Remote Sensing of Environment*, **48**, 159–171.

LOPES, A., NEZRY, E., TOURZI, R., and LAUR, H., 1990. Maximum a posteriori speckle filtering and first order texture models in SAR images. *Proceedings of International Geoscience and Remote Sensing Symposium '90, 20–24 May 1990, College Park, MD, USA* (Piscataway, NJ: IEEE), pp. 2409–2412.

MA, Y. Z., and ROYER, J. J., 1988, Local geostatistical filtering: application to remote sensing. *Sciences de la Terre, Série Informatique*, **27**, 17–36.

MATHERON, G., 1982, *Pour une Analyse Krigeante de Données Régionalisées*. Publication N-732, Centre de Géostatistique, Ecole des Mines de Paris, Fontainebleau.

RICHARDS, J. A., 1986, *Remote Sensing Digital Image Analysis* (New York: Springer-Verlag).

ULABY, F. T., MOORE, R. K., and FUNG, A. K., 1982, *Microwave Remote Sensing, Active and Passive, Volume II: Radar Remote Sensing and Surface Scattering and Emission Theory* (Norwood: Artech House Inc.)

VERHOEST, N. E. C., TROCH, P. A., PANICONI, C., and DE TROCH F. P., 1998, Mapping basin scale variable source areas from multitemporal remotely sensed observations of soil moisture behavior. *Water Resources Research*, **34**, 3235–3244.

WACKERNAGEL, H., 1988, Geostatistical techniques for interpreting multivariate spatial information. In *Quantitative Analysis of Mineral and Energy Resources*, edited by C. F. Chung, A. G. Fabbri and R. Sinding-Larsen (Dordrecht: Reidel), pp. 393–409.

WACKERNAGEL, H., 1998, *Multivariate Geostatistics* (Berlin: Springer-Verlag).

WEN, R., and SINDING-LARSEN, R., 1997, Image filtering by factorial kriging—sensitivity analysis and application to Gloria side-scan sonar images. *Mathematical Geology*, **29**, 433–468.

WONNACOTT, T. H., and WONNACOTT, R. J., 1990, *Introductory Statistics* (New York: Wiley).

WOODCOCK, C. E., STRAHLER, A. H., and JUPP, D. L. B., 1988, The use of variograms in remote sensing: II. real digital images. *Remote Sensing of Environment*, **25**, 349–379.